The DOI for this manuscript is

DOI:10.2151/jmsj.2024-015

J-STAGE Advance published date: February 7th, 2024

Meiyu-Baiu Rainstorm Associated Diurnal Variation and Kinetic Energy Source Analyzed by Multiscale Window Transform–based Energetics Analysis

Ying Wang

School of Marine Sciences, Nanjing University of Information Science and Technology, Nanjing, China

Submitted to ***Journal of Meteorological Society of Japan***

Corresponding Author: Dr. Ying Wang, wangying_thw@nuist.edu.cn

Abstract

The Meiyu-Baiu front is the main weather system that influences the Yangtze-Huai River area of China in early summer. Convective cells along the Meiyu-Baiu front are very active and often lead to regional flooding disasters. In this study, the multiscale window transform (MWT) and MWT-based multiscale energetics analysis are utilized to investigate the dynamic energy transfers during a typical Meiyu-Baiu rainstorm. It is found that baroclinic instability in the lower stratosphere is possibly a primary trigger for the rainstorm and its diurnal variation. The kinetic energy source for single rainstorm case varies in its evolution. During shallow convection, the rainstorm itself is a kinetic energy (KE) source. The baroclinic canonical transfer from the rainstorm window brings a lot of available potential energy (APE) to the background flow window, and is further converted into the background flow KE. In contrast, during deep convection, the primary source of KE is the background flow. The barotropic canonical transfer from the background flow contributes to the APE, thus bringing KE into the rainstorm. Implications on Meiyu-Baiu rainstorm forecasting are also discussed.

Key words: Meiyu-Baiu rainstorm, Diurnal variation, Multiscale window transform, Canonical transfer, Barotropic/Baroclinic instability

1. Introduction

The Meiyu-Baiu front, characterized by a quasi-stationary structure located along the northwestern rim of the North Pacific subtropical anticyclone (NPSA), is the main weather system that extends from the Yangtze River basin in China to Japan from mid-June to mid-July (e.g., Cho and Chen, 1995). This subtropical front has thick moist neutral stratification on the southern flank and a sharp poleward moisture decrease (Ninomiya, 1984). Convective cells along the Meiyu-Baiu front are very active (Nimomiya, 2000; Nimomiya and Shibagaki, 2007; Liu et al., 2004) and can give rise to sudden heavy rainstorms, invoking severe flooding and subsequently great economic loss.

Previous studies have indicated that the Meiyu-Baiu front has weaker baroclinicity over China than over Japan. The moisture gradient is obvious, but the thermal gradient is not (Chen and Chang, 1980). In a weak baroclinic environment, the formation of Meiyu-Baiu rainstorms relies on the interaction among multiscale system components (Ding et al., 2007; Jiang and Ni, 2003). For example, the zonal cloud band usually contains meso-α- and meso-β-scale convective cells. When a rainstorm occurs, there is a stationary trough and ridge at higher latitudes. In the mid-latitudes, the advection of warm air on the eastern edge of the Tibetan Plateau can give rise to convection in southeastern China by inducing adiabatic ascending movement along the westerlies (Ding et al., 2007; Ding, 1991; Zhu et al., 2007). A mass imbalance can be caused by the difference in moisture along the southern and northern parts of the Meiyu-Baiu front, and small-amplitude gravity waves arise that can organize convective cells along the front (Zhao et al., 2011). The magnitude of a Meiyu-Baiu rainstorm is believed to be determined by the convective nonadiabatic heating of mesoscale systems (Sampe and Xie, 2010), but the geometric and dynamic characteristics are still not well understood due to the lack of fine-scale observations. Refined numerical simulations by non-hydrostatic high-resolution numerical weather prediction (NWP) models can effectively make up for the lack of observational data. Based on numerical simulations, the multiscale characteristics of the Meiyu-Baiu system have been investigated in previous studies (e.g., Kawatani and Takahashi, 2003; Zhang et al., 2004; Li et al., 2005; Sun et al., 2007; Ni and Zhou, 2004; Liao and Tan, 2005; Long and Cheng, 2004; Shen et al., 2011; Chen and Gao, 2006; Chen and Qian, 2006; Zhao et al., 2011). Liao and Tan (2005) conducted a case study of a Meiyu-Baiu rainstorm using a simulation by the fifth generation NCAR/Penn State Mesoscale Model (MM5) to investigate the influence of interaction between weather systems at different scales. They found that there are mainly four vertical circulations near the Meiyu-Baiu front. Dynamic and structural characteristics of these circulations vary in different stages during rainstorm evolution. Zhao et al. (2011) utilized the Weather Research and Forecasting (WRF) model to simulate a Meiyu-Baiu rainstorm. The meso-α-, meso-β-, and meso-γ-scale systems were separated by a spatial band-pass filter based on a Morlet wavelet transform, and then three-dimensional dynamic and thermodynamic structural features were analyzed. Their results indicate that there are significant dynamic and thermodynamic differences among these three mesoscale systems in both the horizontal and vertical directions. Meso-α- and meso-β-scale systems have obvious vertical circulations, while meso-γ-scale systems usually develop within a meso-α- or meso-β-scale system, with a characteristic inertial gravity wave. Despite these efforts to understand the dynamic and thermodynamic features of the Meiyu-Baiu front, previous researches have focused mostly processes on one individual scale.

Recently, the multiscale issue has caught much attention in the Meiyu-Baiu research. Fu et al. (2018) applied a temporal scale separation method developed by Murakami (2011) to a case study. They decomposed the original flow into a precipitation-related eddy flow and its background circulation, and utilized the Climate Forecast System version 2 (CFSv2) data of the National Centers for Environmental Prediction (NCEP) to calculate the energy budget within the rainstorm process. Because of the low temporal resolution of the CFSv2 data, their research was focused mainly on a weekly temporal scale with a coarser spatial resolution, which may have led to the underestimation of energy transport. Besides, Meiyu-Baiu rainstorms have a short lifetime, ranging from minutes to a few hours, hence a low temporal resolution may fail to capture the realistic features. Moreover, the method by Murakami (2011) is based on the classical Reynolds decomposition, which does not apply to nonstationary background flow. This, among other problems, motivates us to seek for a more sophisticated methodology to analyze the multiscale interactions associated with the Meiyu-Baiu system.

Ever since the concept of available potential energy was promoted by Lorenz (1955), energetic analysis has been a powerful diagnostic tool in atmospheric and oceanic research (e.g., Dickinson 1969; Charney and Drazin 1961; Lorenz, 1972; Orlanski and Katzfey, 1991; Chang 1993; Hoskins et al., 1983; Trenberth 1986; Liang and Robinson, 2005; Su et al., 2016; Liang 2016). However, Lorenz's energy equation is in a global integration form, which cannot be used for diagnosing regional processes, to which rainstorms are belonging. In order to establish a faithful local Lorenz-type energetics formalism, two issues must be fixed: 1) how to separate transport and transfer processes out of the nonlinear terms in the resulting multiscale energy equations, and 2) how to characterize the temporal variation of the resulting multiscale energy, while applying scale decomposition in the time direction. These issues are resolved in a unified treatment within the framework of multiscale window transform (MWT), a functional analysis tool recently invented by Liang and Anderson (2007). In this study, we will employ MWT and MWT-based multiscale energetics analysis to investigate the dynamic multiscale interactions associated with a Meiyu-Baiu rainstorm. A brief introduction to MWT and MWT-based methodology is provided in section 2. Section 3 introduces the data and experimental design. Results are given in Section 4. Section 5 offers a discussion. A summary is provided in section 6.

2. Methodology

a. Multiscale window transforms

Details regarding MWT have been addressed by Liang and Anderson (2007). MWT is a new functional tool developed to generalize the classical mean-eddy decomposition in fluid mechanics to include three or more ranges of scales, and to ensure a faithful representation of localized energy processes (Liang and Anderson, 2007). It has been utilized to investigate blocking high (Li et al., 2020) and squall line convection, basing on the nonhydrostatic framework simulation by WRF (Guo and Liang, 2022). MWT can decompose a function space into a direct sum of orthogonal subspaces, referring to scale windows. In our case study, five related variable fields (e.g., potential temperature, geopotential, zonal wind, meridional wind, and vertical wind at pressure coordinates) are utilized to present the dynamic features and calculate the energy transfer of a Meiyu-Baiu rainstorm. We decompose these fields into three scale windows: the background flow window, the mesoscale window, and the rainstorm window.

b. MWT-based multiscale energetics

MWT-based multiscale energy analysis utilizes the decomposing fields processed in a former MWT procedure to further calculate some diagnosed variables that can be employed in dynamic process investigation. Detailed derivations of the equations can be found in Liang (2016, Section 4). Here, we just introduce some formulas and clarify their meteorological meanings when applied in the following discussion.

Kinetic energy (KE) is an essential variable to be diagnosed during rainstorm dynamic analysis. For every scale window, kinetic energy is calculated by two-dimensional horizontal wind as follows:

$$K^{\varpi} = \frac{1}{2}\hat{\mathbf{v}}_h^{\sim\varpi} \cdot \hat{\mathbf{v}}_h^{\sim\varpi} \tag{1}$$

K^{ϖ} is the kinetic energy in scale window ϖ. $\hat{\mathbf{v}}^{\sim\varpi}$ and $\hat{\mathbf{v}}_h^{\sim\varpi}$ are three-dimensional wind and two-dimensional horizontal wind in scale window ϖ, respectively. Then, the flux of KE in window ϖ is presented as

$$\mathbf{Q}_K^{\varpi} = \frac{1}{2}\widehat{(\mathbf{v}\mathbf{v}_h)}^{\sim\varpi} \cdot \hat{\mathbf{v}}_h^{\sim\varpi} \tag{2}$$

For the transfer of KE between different scale windows, canonical transfer is introduced here. The canonical transfer of KE from the background flow window to the mesoscale window can present barotropic instability, which is a tool for investigating dynamic processes. Canonical transfer of KE to window ϖ is

$$\Gamma_K^{\varpi} = \frac{1}{2}\left[\widehat{(\mathbf{v}\mathbf{v}_h)}^{\sim\varpi} : \nabla\hat{\mathbf{v}}_h^{\sim\varpi} - \nabla\cdot\widehat{(\mathbf{v}\mathbf{v}_h)}^{\sim\varpi}\cdot\hat{\mathbf{v}}_h^{\sim\varpi}\right] \tag{3}$$

We calculate pressure flux in window ϖ as

$$\mathbf{Q}_P^{\varpi} = \hat{\mathbf{v}}^{\sim\varpi}\widehat{\Phi}^{\sim\varpi} \tag{4}$$

Here, $\widehat{\Phi}^{\sim\varpi}$ is the geopotential in window ϖ.

APE, which is usually the source of KE, is also diagnosed. APE is presented as

$$A^{\varpi} = \frac{1}{2}c\left(\hat{T}^{\sim\varpi}\right)^2 \tag{5}$$

$$c = \frac{g}{\bar{T}(g/c_p - L)} \tag{6}$$

$\hat{T}^{\sim\varpi}$ is the potential temperature in window ϖ, and c_p is specific heat at constant pressure. $L = \frac{\partial \bar{T}}{\partial z}$ is the lapse rate, and g is acceleration of gravity. The buoyancy conversion rate, which indicates the conversion rate from KE to APE, is calculated as

$$b^{\varpi} = \widehat{\omega}^{\sim\varpi}\widehat{\alpha}^{\sim\varpi} \tag{7}$$

ω is the vertical wind in pressure coordinates and α is the reciprocal of density. APE flux in scale window ϖ is calculated as

$$\mathbf{Q}_A^{\varpi} = \frac{1}{2}c\hat{T}^{\sim\varpi}(\widehat{\mathbf{v}T})^{\sim\varpi} \tag{8}$$

Similar to canonical transfer of KE, canonical transfer of APE from the background flow window to the mesoscale window can present baroclinic instability. Here, we get canonical transfer of APE to window ϖ as

$$\Gamma_A^{\varpi} = \frac{c}{2}[(\widehat{\mathbf{v}T})^{\sim\varpi} \cdot \nabla\hat{T}^{\sim\varpi} - \hat{T}^{\sim\varpi}\nabla \cdot (\widehat{\mathbf{v}T})^{\sim\varpi}] \tag{9}$$

Then, the apparent source/sink, which is usually negligible, is calculated as

$$S_A^{\varpi} = \frac{1}{2}\hat{T}^{\sim\varpi}(\widehat{\omega T})^{\sim\varpi}\frac{\partial c}{\partial p} + \frac{1}{\bar{T}}(\widehat{\omega\alpha})^{\sim\varpi} \tag{10}$$

Finally, the multiscale kinetic and available energy equations are

$$\frac{\partial K^{\varpi}}{\partial t} + \nabla \cdot \mathbf{Q}_K^{\varpi} = \Gamma_K^{\varpi} - \nabla \cdot \mathbf{Q}_P^{\varpi} - b^{\varpi} + F_{K,p}^{\varpi} + F_{K,h}^{\varpi} \tag{11}$$

$$\frac{\partial A^{\varpi}}{\partial t} + \nabla \cdot \mathbf{Q}_A^{\varpi} = \Gamma_A^{\varpi} + b^{\varpi} + S_A^{\varpi} + F_A^{\varpi} \tag{12}$$

Here, $F_{K,p}^{\varpi}$ and $F_{K,h}^{\varpi}$ are the residue items of the KE equation. S_A^{ϖ} is the apparent source/sink of A^{ϖ} and is usually negligible. F_A^{ϖ} is the residue item of the APE equation.

3. WRF Simulation and Validation

With an advanced research version of the Weather Research and Forecasting (WRF) model (Version 3.9.1, Skamarock et al., 2008), a high-resolution numerical simulation of a Meiyu-Baiu rainstorm that occurred during 27-28 June 2016 was conducted. NCEP FNL (Final Operational Global Analysis) data were utilized to provide the initial and boundary conditions for the WRF simulation. A single domain covered the main area of the Meiyu-Baiu front at a horizontal resolution of 3 km. The number of horizontal grid points was 550×450, with the center of the model domain at 117.5 °E, 31.0 °N. There were 51 vertical sigma levels, and the top of the model was at 10 hPa. The model output was saved in 10-min intervals. The physical parameterization schemes used for the simulation were the WSM (WRF Single-Moment) 6-class graupel scheme (Hong and Lim, 2006), RRTM (Rapid and accurate Radiative Transfer Model) longwave radiation scheme (Mlawer et al., 1997), Goddard shortwave scheme (Chou and Suarez, 1999), Monin-Obukhov (Janjić) surface-layer scheme (Janjić, 2002; Mellor and Yamada, 1982), RUC (Rapid Update Cycle) land-surface scheme (Smirnova et al., 1997), and Mellor-Yamada-Janjić (MYJ) TKE (Turbulent Kinetic Energy) boundary-layer scheme (Janjić, 2002). The cumulus parameterization scheme was not used.

The simulation experiment starts at 1800 UTC 26 June 2016, with an integration period of 54 h. The initial 6 h simulation is treated as a spin-up. The valid simulation from 0000 UTC 27 June to 0000 UTC 29 June 2016 is used for analysis. For this study case, a gusty Meiyu-Baiu rainstorm occurred from 1200 UTC 27 to 0900 UTC 28 June.

To validate the simulation, the 21 h (between 1200 UTC 27 and 0900 UTC 28 June) accumulated precipitation is shown in Figure 1 against the merged product of satellite-derived precipitation from CMORPH (the Climate Prediction Center MORPHing technique) and hourly precipitation observed at the automatic weather stations in China. The merged data are utilized as observations, which can correctly capture the main spatial characteristics of short-duration heavy rainfall, with 1 h temporal resolution and 0.1 ° spatial resolution (Zhou et al., 2015). PDF (Possibility Density Function) and OI (Optimum Interpolation) are employed within the merged algorithm. Figure 1 shows that the simulated precipitation patterns are similar to the observations, with the rain belt located from northern Hunan province to southern Jiangsu province. Two sensitive domains, with maximum rainfall greater than 80 mm, are chosen to investigate the multiscale energetic processes during the rainstorm. They are in northern Hunan province (Domain A) and southern Anhui province (Domain B), respectively. Detailed synoptic characteristics can be captured in Figure 2. The synoptic pattern is a typical one that the northwestern rim of the North Pacific subtropical anticyclone locates along the Yangtze River, together with a cold vertex at higher latitude. Two surface pressure troughs, respectively locate at domain A and B, could invoke upward movement. Additionally, abundant transportation of water vapor by Low Level Jet and instability of low troposphere in the northern part of Low Level Jet contribute a lot to the occurrence of rainstorm. The simulated geopotential heights at 100hPa, 500 hPa, and 700 hPa are presented in Figure 3. Similar synoptic characteristics can be captured. During this rainstorm, geopotential height troughs locate in Domain A and B (Figure 3(c2)). At 100 hPa, the geopotential height decreases and shear vorticity judged from the wind vectors increases, both in Domain A and B (Figure 3(a2)). With the favor of such synoptic background, convection is clearly seen with the maximum reflectivity over than 35 dBZ from 1800 UTC to 0600 UTC 28 June (Figure 4).

4. Multiscale energetics analysis

Five related variable fields from the simulation, namely potential temperature, geopotential, zonal wind, meridional wind, and vertical wind in pressure coordinates, are interpolated to 20 pressure levels (ranging from 1000 hPa to 10 hPa) vertically and 0.03 ° horizontally, and are then processed in the MWT framework. WRF outputs provide consistent simulated fields with 256 time series from 0000 UTC 27 June to 1830 UTC 28 June in a 10 min interval. As precipitation phenomena is greatly associated with vertical velocity, the values of time ranges for the decomposed windows are adopted basing on the temporal scale for meso-scale systems along Meiyu-Baiu front and spectrum of simulated vertical velocity at 700 hPa (Figure 5). Then, WRF simulations are decomposed into three temporal scale windows: the background flow window (from 21.33 h to 42.67 h, window 0), the mesoscale window (from 5.33 h to 21.33 h, window 1), and the rainstorm window (from 20 min to 5.33 h, window 2). The MWT-based multiscale energetic analysis within the defined sensitive domains (A and B in Figure 1) is discussed in this study.

a. Rainstorm diurnal variation

Meiyu-Baiu rainstorms typically have diurnal variation in the amount and intensity of precipitation. Previous studies have attempted to find a proper way to explain this diurnal variation (e.g., Zhou et al., 2008; Bao et al., 2011; Xue et al., 2018). The effect of nocturnal low-level jets (LLJs) is considered to be the main factor leading to diurnal variation in precipitation (Wallace, 1975; Helfand and Schubert, 1995; Carbone and Tuttle, 2008; Sato, 2013), with emphasis on the boundary layer. Xue et al. (2018) explained the diurnal variation in Meiyu-Baiu precipitation with the Blackadar boundary layer inertial oscillation theory, considering its convergence forcing by low-level ageostrophic winds. In this study, obvious diurnal variation in the rainstorm is observed in both of the sensitive domains, with an early morning peak (Figure 6). Equipped with the new methodology, we anticipate new insights to explain this diurnal variation.

We first examine the vertical structure of the diurnal variation. Vertical velocity and geopotential height are used to illustrate the dynamic patterns (Figures 7-8). In all three scale windows, vertical velocity shows an oscillating pattern with time. When strong precipitation occurs, an obvious negative signal (i.e., representing vertical upward movement) exists in the background flow window from 850 hPa to 350 hPa, corresponding well to the precipitation peak phase in Figure 6. For the geopotential field, the lower layer and upper layer of troposphere separately occupies an opposite signal, with an oscillation about 12 hours in the mesoscale window. In the background flow window, high geopotential values occur mainly above 500 hPa. Several hours before the rainstorm, the upper boundary around 100 hPa in the background flow window shows a downward movement and forms a time-dimensional trough during the rainstorm peak period, which may reflect some dynamic processes at the top of the troposphere.

We now investigate these dynamic processes. Among the multiscale energetics as shown in section 2, the canonical transfers Γ_A^{ϖ} and Γ_K^{ϖ} can figure important processes in the multiscale interactions. It has been rigorously proved that they quantitatively measure the two fundamental instabilities, namely, baroclinic instability and barotropic instability, in geophysical fluid dynamics (Liang and Robinson, 2005). Figure 9 illustrates the baroclinic canonical transfer in different windows. In Figure 9 (a1) and (a2), there is an obvious baroclinic canonical transfer from the background flow window to the mesoscale window at 100 hPa, which indicates a baroclinic instability above the top of the troposphere. About 5 h before the rainstorm, the baroclinic canonical transfer gains a high value of more than 0.3 $\mathrm{m^2 \cdot s^{-3}}$, which lowers when the rainstorm occurs. The baroclinic canonical transfer from the background flow window to the rainstorm window presents a similar pattern above the top of the troposphere. For the mesoscale window, there also exists a baroclinic canonical transfer to the rainstorm window, forming a secondary instability. These three baroclinic canonical transfers all offer an instable dynamical environment in the lower stratosphere before rainstorm. The barotropic canonical transfers are shown in Figure 10. During the rainstorm, the rainstorm window and mesoscale window always gain barotropic canonical transfer from the background flow window, with a positive to negative vertically staggered pattern in the troposphere. In the vertical shallow convective region in particular (height about 4 km), barotropic instability is obvious within both of the sensitive domains (Figure 10 (a1) and (a2)), which seems to be in accord with the weak baroclinicity of Meiyu-Baiu front.

b. Kinetic energy source

APE can be released and largely converted into the KE of horizontal wind through vertical motion, under conditions closely approximating hydrostatic equilibrium (Kuo, 1954; White and Saltzman, 1956). Therefore, the release of APE is an essential factor associated with convective rainfall (Eshel and Farrell, 2001; Murugavel et al., 2011; Chen et al., 2014; Zhang et al., 2019). Figure 11 illustrates the buoyancy conversion rate, with a minus sign added. Thus, the positive value indicates the conversion from APE to KE. For the background flow window, the conversion from APE to KE occurs mainly in the middle to high levels of the troposphere. With the development of the convective rainstorm, the buoyancy conversion rate signal separates into two branches for the rainstorm window. The lower one is stable at 700 hPa and the higher one goes up to a higher vertical level, about 200 hPa, which indicates a region of severe vertical convection. The same KE pattern can be captured in the rainstorm window in Figure 12. Diabatic heating is another factor to be considered in the Meiyu-Baiu rainstorm process. The contribution of vapor latent heating cannot be ignored. Liang (2016) indicates that the contribution of vapor latent heating is contained in F_A^{ϖ}. The vertical distribution of F_A^{ϖ} is shown in Figure 13. In these three scale windows, vapor latent heating is apparent during the rainstorm above 700 hPa, inside convective clouds. With the release of the vapor latent heat, APE is reserved for further conversion into KE.

Discussed above is about the spatiotemporal distributions of the baroclinic and barotropic canonical transfers, APE/KE tendencies, and buoyancy conversion. The vertical integration of them would provide a quantified Lorenz energy cycle and further clarify the KE source for Meiyu-Baiu rainstorms. Because baroclinic canonical transfer and barotropic canonical transfer (shown in Figures 9 and 10) differ in the lower level and above the top of the troposphere, we employ 300 hPa as a boundary to separate the vertical coordinate into an upper and a lower component to be integrated and then provide the Lorenz energy circulation chart of these two sensitive domains (shown in Figure 14), respectively. Below 300 hPa, the direction of energy flow is similar in both of the sensitive domains. Baroclinic canonical transfers from the rainstorm window and mesoscale window accumulate a large amount of APE, which will further convert into KE in the background window, forming the main KE source. Moreover, for the rainstorm window, there is direct barotropic canonical transfer from the background flow window and mesoscale window. Buoyancy conversion, gaining KE from APE with energy release within the rainstorm window, contributes over 39% of the KE in the rainstorm window. Above 300 hPa, where severe vertical convection reaches such a height, the rainstorm window turns into the sink of APE, which converts to KE with buoyancy conversion. Additionally, barotropic canonical transfer from the background flow window directly brings a lot of KE to the rainstorm window.

Based on the discussion above, Figure 15 provides a conceptual model of the KE source for the Meiyu-Baiu rainstorm. For shallow convection, the rainstorm window is the KE source. Baroclinic canonical transfer from the rainstorm window brings a lot of APE, which is further converted into KE in the background flow window. For severe convection, with convective height higher than 300 hPa, the main source of KE is the background flow window. Barotropic canonical transfer brings KE from the background flow window to the rainstorm window. Baroclinic canonical transfer from the background flow window also contributes to APE, which can be converted into KE within the rainstorm window.

5. Discussion

In the above analysis about baroclinic and barotropic instabilities, an obvious baroclinic instability signal can be captured around 100 hPa a few hours before the rainstorm. Is there any relationship between the upper-level disturbances and rainstorm occurrence? Baroclinic instability in the upper troposphere could generate mesoscale gravity waves, the period of which is 0.5-4 h (Zhang, 2004). Mesoscale gravity waves are found intimately linked to the initiation and modulation of convection (Lane and Reeder, 2001; Zhang et al., 2001). In Figure 3, an upper-level jet streak exists north of these two domains at 100 hPa. Then, such wind shear instability would generate mesoscale gravity waves, which possibly linked to geostrophic adjustment associated with an unbalanced upper-tropospheric jet (Zhang, 2004). In Figure 16, the evolution and baroclinic structure of mesoscale gravity wave can be captured. As the simulation resolution is 3 km, a refined mesoscale gravity wave structure is presented. Horizontal distribution of straightly oscillated convergence and divergence signals clearly present the structure of mesoscale gravity wave, with an approximately wavelength of 30 km. From t=36 to t=60, approximately 4.2 h which corresponds well with baroclinic instability signal leading time against the rainstorm occurrence in Figure 9, the mesoscale gravity waves propagate downward from lower stratosphere to lower troposphere, with a baroclinic pattern. Once propagating to the lower troposphere, it perturbs the flow and helps to organizing convection. During the rainstorm (t=120), large amount of convection has been triggered, with a barotropic structure, fitting well with the barotropic instability shown in Figure10. Additionally, the domain averaged positive divergence signal spreads downward from 100 hPa, acting as a pump to suck the lower-layer air and trigger the rainstorm (Figure 17). Overall, the mechanism of diurnal variation in the Meiyu-Baiu rainstorm is a complex interaction between the upper and lower layers of the troposphere. To this case study, baroclinic instability in the lower stratosphere is possibly the primary trigger for the diurnal variation of the Meiyu-Baiu rainstorm in both of the sensitive regions.

In previous studies, the effect of nocturnal low-level jets (LLJs) is considered to be the main factor leading to diurnal variation in precipitation, with emphasis on the boundary layer. In our case study, the effect of LLJ is really important within the rainstorm period. In Figure 2 and Figure 3, southwesterly winds at 700-hPa level flowed into the rainfall areas at 0000 UTC 28 June, nearly the peak time of the rainstorm (Figure 6). At 1200 UTC 27 June, the southwesterly winds were not constructed. Additionally, vapor latent heating which is contained in the residual term is apparent during the rainstorm above 700 hPa in the rainstorm period (Figure 13). However, the baroclinic instability signal in the upper level upper occurred 5 h before rainstorm. Although its magnitude is not comparable with that of the residual term, the downward propagating mesoscale gravity wave helps to the initiation and organization of convection. Moisture inflow in the lower levels is a quite important factor within rainstorm period. The upper level baroclinic instability offers a perturbation, which helps to organize convection. Without convection, abundant moisture would not lead to rainstorm occurrence. These two factors are both essential. With the newly energetics analysis tool, we captured the upper level signal, which possibly excites the rainstorm occurrence. For only one case study, the result may be insufficient. In the future, the robustness of rainstorm occurrence excited by upper level baroclinic instability should be tested, basing on a refined simulation with a longer period and more rainstorm cases.

6. Summary

The Meiyu-Baiu front is the main weather system that influences the Yangtze-Huai River area, China, in early summer. The formation of Meiyu-Baiu front rainstorms relies on the multiscale interactions in weather system. With a recently developed energetics analysis (Liang and Robinson, 2005; Liang, 2016), which is based on a functional analysis tool namely multiscale window transform (MWT), a rainstorm case is investigated to determine the energy transfer between different scale windows. Related highly resolved fields generated from a WRF model are decomposed using MWT into parts on the background flow window, mesoscale window, and rainstorm window. The interactions between these windows are then quantitatively analyzed in terms of the energy transferred between them. This offers an energetic view of the diurnal variation and kinetic energy source for the Meiyu-Baiu rainstorm. Listed in the following are the main conclusions.

(a) An obvious baroclinic canonical transfer from the background flow window to the mesoscale window and rainstorm window occurs at about 100 hPa, 5 h before the Meiyu-Baiu rainstorm. The oscillation of the baroclinic canonical transfer agrees well with the diurnal variation of the rainstorm.

(b) Baroclinic instability in the lower stratosphere is possibly the primary trigger for the rainstorm to this case study. Baroclinic instability in the upper troposphere can generate mesoscale gravity waves. The mesoscale gravity waves propagate downward from lower stratosphere to lower troposphere, with a baroclinic pattern. Once propagating to the lower troposphere, it perturbs the flow and helps to organizing convection.

(c) The main source of KE during the Meiyu-Baiu rainstorm with a convective height lower than 10 km is baroclinic canonical transfer from the rainstorm window, which further converts to KE within the background flow window. Moreover, the main source of KE for severe convection above 300 hPa is barotropic canonical transfer from the background flow window and baroclinic canonical transfer from the background flow window, which further converts to KE within the rainstorm window.

In short, the MWT-based multiscale energetics analysis offers a new insight into the diurnal variation and kinetic energy source in a typical Meiyu-Baiu rainstorm. Canonical transfer of APE from the background flow window to the mesoscale window can present baroclinic instability. Baroclinic instability is associated with mesoscale gravity waves, the period of which is 0.5-4 h, fitting well with the leading time of baroclinic signal before rainstorm. Thus, baroclinic instability in the lower stratosphere is the primary trigger for rainstorm occurrence, which could be a powerful dynamic precursor that would be useful for forecasting. Barotropic canonical transfer together with baroclinic canonical transfer explains the kinetic energy source during different convective stages. We are expecting to apply the MWT-based multiscale energetic tool to more Meiyu-Baiu rainstorm cases and its successes in more operational forecasting applications.

Acknowledgments

The author appreciates NCAR for developing and updating the WRF model. The author is grateful to Prof. X. San Liang at Fudan University, Prof. Zhaoxia Pu at University of Utah and Prof. Ronghua Zhang at Nanjing University of Information Science and Technology for helpful discussion and useful comments. This work is supported by the National Science Foundation of China (NSFC) under Grant 41905089, the China Scholarship Council (CSC) Program (201908320156), and the NUIST Startup Program (2017r076).

Data Availability Statement

NCEP FNL data can be achieved from the website (https://rda.ucar.edu/datasets/ds083.2), and the merged precipitation data can be obtained from the website (http://data.cma.cn/data/cdcdetail/dataCode/SEVP_CLI_CHN_MERGE_CMP_PRE_HOUR_GRID_0.10.html)

References

Bao, X., F. Zhang, and J. Sun, 2011: Diurnal variations of warm-season precipitation east of the Tibetan Plateau over China. *Mon. Wea. Rev.*, **139**(9), 2790–2810, doi: 10.1175/MWR-D-11-00006.1

Carbone, R. E., and J. D. Tuttle, 2008: Rainfall occurrence in the United States warm season: The diurnal cycle. *J. Clim*., **21(16)**, 4132-4146, https://doi.org/10.1175/2008JCLI2275.1

Chang, E. K. M., 1993: Downstream development of baroclinic waves as inferred from regression analysis. *J. Atmos. Sci.*, **50** (13), 2038–2053, https://doi.org/10.1175/1520-0469(1993)050<2038:DDOBWA>2.0.CO;2

Charney, J. G., and P. G. Drazin, 1961: Propagation of planetary scale disturbances from the lower into the upper atmosphere. *J. Geophys. Res*., **66**, 83–109, doi:10.1029/JZ066i001p00083.

Chen, G.-X., R. Yoshida, W.-M. Sha et al., 2014: Convective instability associated with the eastward-propagating rainfall episodes over eastern China during the warm season. *J. Clim*., **27**, 2331-2339, doi: 10.1175/JCLI-D-13-00443.1

Chen, L.-F., and K. Gao, 2006: The simulation of the uneven characteristics of Meiyu front structure. *Acta Meteor. Snica*, **64(2)**, 164-179.

Chen, T.-J. G., and C.-P. Chang, 1980: The structure and vorticity budget of an early summer monsoon trough (Mei-Yu) over southeastern China and Japan. *Mon. Wea. Rev.*, **108**, 942–953, https://doi.org/10.1175/1520-0493(1980)108<0942:TSAVBO>2.0.CO;2

Chen, Y.-M., and Y.-P. Qian, 2006: The analysis and numerical simulation of atmospheric circulation of Mei-yu rainfall in the mid-lower reaches of the Changjiang River. *J. Tropical Meteor*., **22(1)**, 26-33.

Cho, H.-R., and T.-J. G. Chen, 1995: Mei-Yu frontogenesis. *J. Atmos. Sci.*, **52**, 2109–2120, https://doi.org/10.1175/1520-0469(1995)052<2109:MYF>2.0.CO;2

Chou, M.-D., and M. J. Suarez, 1999: A solar radiation parameterization for atmospheric studies. *NASA Tech. Memo*, 104606, 40.

Dickinson, R. E., 1969: Theory of planetary wave-zonal flow interaction. *J. Atmos. Sci*., **26**, 73-81, doi:10.1175/1520-0469(1969)026,0073:TOPWZF.2.0.CO;2.

Ding, Y.-H., 1991: Advanced Meteorology. Beijing, *Meteorological Press*, 236.

Ding, Y.-H., J.-J. Liu, Y. Sun et al., 2007: A study of the synoptic-climatology of the Meiyu system in East Asia. *Chinese J. Atmos. Sci.*, **31(6)**, 1082-1101.

Eshel, G., and B. F. Farrell, 2001: Thermodynamics of eastern Mediterranean rainfall variability. *J. Atmos. Sci.*, **58**, 87–92, https://doi.org/10.1175/1520-0469(2001)058<0087:TOEMRV>2.0.CO;2

Fu, S., R.-X. Liu, and J.-H. Sun, 2018: On the scale interactions that dominate the maintenance of a persistent heavy rainfall event: A piecewise energy analysis. *J. Atmos. Sci.*, **75**, 907-925, doi: 10.1175/JAS-D-17-0294.1.

Guo, Ziyu, X. San Liang, 2022: Nexus of ambient flow and squall line via turbulence in the March 2018 meso-scale convective system over Southeast China. Atmospheric Research, 277, 106287. doi: 10.1016/j.atmosres.2022.106287

Helfand, H. M., and S. D. Schubert, 1995: Climatology of the simulated Great Plains low-level jet and its contribution to the continental moisture budget of the United States. *J. Clim*., **8(4)**, 784-806, https://doi.org/10.1175/1520-0442(1995)008<0784:COTSGP>2.0.CO;2

Hong, S.-Y., and J.-O. J. Lim, 2006: The WRF Single-Moment 6-Class Microphysics Scheme (WSM6). *J. Korean Meteorol. Soc*. 2006, **42**, 129–151.

Hoskins, B. J., J. Brian, I. N. James, and G. H. White, 1983: The shape, propagation and mean-flow interaction of large-scale weather systems. *J. Atmos. Sci*., **40**, 1595–1612, doi:10.1175/1520-0469(1983)040,1595:TSPAMF.2.0.CO;2.

Janjić, Z. I., 2002: Nonsingular implementation of the Mellor–Yamada level 2.5 scheme in the NCEP Meso model. *NCEP Office Note*, 437, 61.

Jiang, J.-Y., and Y.-Q. Ni, 2003: A diagnostic study of the multi-scale characteristics of a Meiyu front heavy rain-fall process in 1998. *Acta Meteor. Snica*, **61(6)**, 673-683.

Kawatani, Y., and M. Takahashi, 2003: Simulation of the Baiu front in a high resolution AGCM. *J. Meteor. Soc. Japan*, **81**, 113–126.

Kuo, H. L., 1954: Energy releasing processes and stability of thermally driven motions in a rotating fluid. *J. Meteorol.*, **13**, 82-101, https://doi.org/10.1175/1520-0469(1956)013<0082:ERPASO>2.0.CO;2

Lane, T. P., and M. J. Reeder, 2001: Convectively generated gravity waves and their impacts on the cloud environment. *J. Atmos. Sci.*, 58, 2427–2440, https://doi.org/10.1175/1520-0469(2001)058<2427:CGGWAT>2.0.CO;2

Li G., J. Ma, X. San Liang, 2020: A study of the multiscale dynamical processes underlying the blocking high that caused the January 2008 freezing rain and snow storm in southern China (in Chinese). *Acta Meteor. Snica.*, **78**(1), 18-32, doi: 10.11676/qxxb2020.016

Li, K., Y.-P. Xu, R.-C. Yu, and R. Cheng, 2005: Comparative studies of three types of heavy rainstorms associated with the Meiyu front by numerical simulations. *Chinese J. Atmos. Sci.*, **29(2)**, 236-248.

Liang, X. S., 2016: Canonical transfer and multiscale energetics for primitive and quasigeostrophic atmospheres. *J. Atmos. Sci.*, **73**, 4439–4468, doi:10.1175/JAS-D-16-0131.1.

Liang, X. S., and A. R. Robinson, 2005: Localized multiscale energy and vorticity analysis: I. fundamentals. *Dyn. Atmos. Oceans*, **38**, 195–230, doi:10.1016/j.dynatmoce.2004.12.004.

Liang, X. S., and D. G. M. Anderson, 2007: Multiscale window transform. *SIAM J. Mutiscale Model. Simul.*, **6(2)**, 437–467, https://doi.org/10.1137/06066895X.

Liao, J., and Z.-M. Tan, 2005: Numerical simulation of a heavy rainfall event along the Meiyu front: Influences of different scale weather systems. *Acta Meteor. Sinica*, **63(5)**, 771-789.

Liu, Y., M. Xu, and H.-F. Zhu, 2004: The study of interannual changes about the Meiyu period in Anhui province. *Scientia Meteor. Sinica*, **24(4)**, 488-494.

Long, X., and L.-S. Cheng, 2004: Numerical simulation and analysis for "99.6" Meiyu front rainstorm and the low vortex with shear line. *Chinese J. Atmos. Sci.*, **28(3)**, 342-356.

Lorenz, E. N., 1955: Available potential energy and the maintenance of the general circulation. *Tellus*, **7**, 157-167, doi:10.1111/j.2153-3490.1955.tb01148.x.

Lorenz, E. N., 1972: Barotropic instability of Rossby wave motion. *J. Atmos. Sci.*, **29**, 258-264. https://doi.org/10.1175/1520-0469(1972)029<0258:BIORWM>2.0.CO;2.

Mellor, G. L., and T. Yamada, 1982: Development of a turbulence closure model for geophysical fluid problems. *Rev. Geophys*. **20**, 851–875.

Mlawer, E. J., S. J. Taubman, P. D. Brown, M. J. Iacono, and S. A. Clough, 1997: Radiative transfer for inhomogeneous atmospheres: RRTM, a validated correlated-k model for the longwave. *J. Geophys. Res. Atmos.*, **102**, 16663–16682.

Murakami, S., 2011: Atmospheric local energetics and energy interactions between mean and eddy fields. Part I: Theory. *J. Atmos. Sci*., **68**, 760–768, https://doi.org/10.1175/2010JAS3664.1.

Murugavel, P., S. D. Pawar, and V. Gopalakrishnan, 2011: Trends of Convective Available Potential Energy over the Indian region and its effect on rainfall. *Int. J. Climatol.*, **32**, 1362–1372, doi: 10.1002/joc.2359.

Ni, Y.-Q., and X.-J. Zhou, 2004: Study for formation mechanism of heavy rainfall within the Meiyu front along the middle and downstream of Yangtze River and theories and methods of their detection and prediction. *Acta Meteor. Sinica*, **62(5)**, 647-662.

Ninomiya, K., 1984: Characteristics of Baiu front as a predominant subtropical front in the summer Northern Hemisphere. *J. Meteor. Soc. Japan,* **62**, 880-894.

Ninomiya, K., 2000: Large- and meso-a-scale characteristics of Meiyu/Baiu front associated with intense rainfalls in 1-10 July 1991. *J. Meteor. Soc. Japan*, **78**, 141–157.

Ninomiya, K., and Y. Shibagaki, 2007: Multi-scale features of the Meiyu-Baiu front and associated precipitation systems. *J. Meteor. Soc. Japan*, **85B**, 103–122.

Orlanski, I. and J. Katzfey, 1991: The life cycle of a cyclone wave in the southern hemisphere. Part I: Eddy energy budget. *J. Atmos. Sci*., **48 (17)**, 1972–1998, https://doi.org/10.1175/1520-0469(1991)048<1972:TLCOAC>2.0.CO;2

Sampe, T., and S-P. Xie, 2010: Large-scale dynamics of the Meiyu-Baiu rainband: Environmental forcing by the westerly jet. *J. Clim.*, **23**, 113-134, doi:10.1175/2009JCLI3128.1.

Sato, T., 2013: Mechanism of orographic precipitation around the Meghalaya Plateau associated with intraseasonal oscillation and the diurnal cycle. *Mon. Wea. Rev.*, **141**, 2451–2466, doi: 10.1175/MWR-D-12-00321.1

Shen, S., Y.-C. Zhang, H. Xiao, and X.-P. Zhou, 2011: Ability of the model BCC_AGCM2.0.1 to reproduce Meiyu precipitation. *Meteor. Mon.*, **37(11)**, 1336-1342.

Skamarock, W. C., J. B. Klemp, J. Dudhia, D. O. Gill, D. M. Barker, W. Wang, and J. G. Powers, 2008: A description of the Advanced Research WRF version 3. NCAR Technical note -

475+STR (2008). Available at http://citeseerx.ist.psu.edu/viewdoc/summary?doi=10.1.1.484.3656

Smirnova, T. G., J. M. Brown, and S. G. Benjamin, 1997: Performance of different soil model configurations in simulating ground surface temperature and surface fluxes. *Mon. Wea. Rev.* **125**, 1870–1884, https://doi.org/10.1175/1520-0493(1997)125<1870:PODSMC>2.0.CO;2

Su, Z., A. Ingersoll, A. Steward, and A. Thompson, 2016: Ocean convective available potential energy. Part II: Energetics of thermobaric convection and thermobaric cabbeling. *J. Phys. Oceanogr*., **46**, 1097–1115, doi:10.1175/JPO-D-14-0156.1.

Sun, J., X.-F. Lou, Z.-J. Hu, and S.-X. Zhao, 2007: A numerical simulation on torrential rain during the Meiyu period and analysis of mesoscale and microscale structure of convective systems. *Chinese J. Atmos. Sci.*, **31(1)**, 1-18.

Trenberth, K. E., 1986: An assessment of the impact of transient eddies on the zonal flow during a blocking episode using localized Eliassen-Palm flux diagnostics. *J. Atmos. Sci*., **43**, 2070–2087, doi:10.1175/1520-0469(1986)043,2070:AAOTIO.2.0.CO;2.

Wallace, J. M., 1975: Diurnal variations in precipitation and thunderstorm frequency over the conterminous United States. *Mon. Wea. Rev.*, **103(5)**, 406-419, https://doi.org/10.1175/1520-0493(1975)103<0406:DVIPAT>2.0.CO;2.

White, R. M., and B. Saltzman, 1956: On conversions between potential and kinetic energy in the atmosphere. *Tellus*, **8**, 357-363.

Xue, M., X. Luo, K.-F. Zhu, Z.-Q. Sun, and J.-F. Fei, 2018: The controlling role of boundary layer inertial oscillations in Meiyu frontal precipitation and its diurnal cycles over China. *J. Geophys. Res. Atoms.,* **123**, 5090-5115, doi: 10.1029/2018JD028368.

Zhang, F., S. E. Koch, C. A. Davis, and M. L. Kaplan, 2001: Wavelet analysis and the governing dynamics of a large-amplitude gravity wave event along the east coast of the United States. *Quart. J. Roy. Meteor. Soc.*, 127 , 2209–2245, https://doi.org/10.1002/qj.49712757702

Zhang, F.-Q., 2004: Generation of mesoscale gravity waves in upper-tropospheric jet–front systems. *J. Atmos. Sci.*, **61**, 440-457, https://doi.org/10.1175/1520-0469(2004)061<0440:GOMGWI>2.0.CO;s.

Zhang, L., J.-Z. Min, and X.-R. Zhuang, 2019: General features of extreme rainfall events produced by MCSs over East China during 2016–17. *Mon. Wea. Rev.*, **147**, 2693–2714, https://doi.org/10.1175/MWR-D-18-0455.1

Zhang, X.-L., S.-Y. Tao, and S.-L. Zhang, 2004: Three types of heavy rainstorms associated with the Meiyu front. *Chinese J. Atmos. Sci.*, **28(2)**, 187-205.

Zhao, Y.-C., Y.-H. Wang, and C.-G. Cui, 2011: Multi-scale structure features of a typical Mei-yu frontal rainstorm process. *Trans. Atmos. Sci*., **34(1)**, 14-27.

Zhou, T., R. Yu, H. Chen, A. Dai, and Y. Pan, 2008: Summer precipitation frequency, intensity, and diurnal cycle over China: A comparison of satellite data with rain gauge observations. *J. Clim*., **21**(16), 3997–4010, doi:10.1175/2008JCLI2028.1.

Zhou, X., Y.-L. Luo, and X.-L. Guo, 2015: Application of a CMORPH-AWS merged hourly gridded precipitation product in analyzing characteristics of short-duration heavy rainfall over southern China. *J. Tropical Meteor.*, **31**(3), 332-344.

Zhu, Q.-G., J.-R. Lin, S.-W. Shou, and D.-S. Tang, 2007: Principles and Methods of Meteorology, Beijing, *Meteorological Press*, 351.

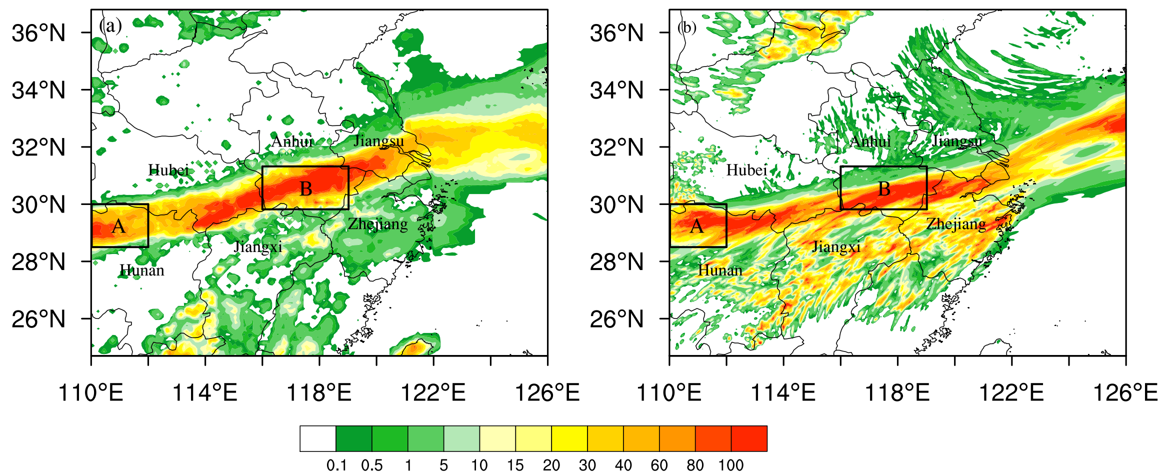

Figure 1. Observed accumulated precipitation (a) and simulated accumulated precipitation (b) from 1200 UTC 27 to 0900 UTC 28 June (unit: mm).

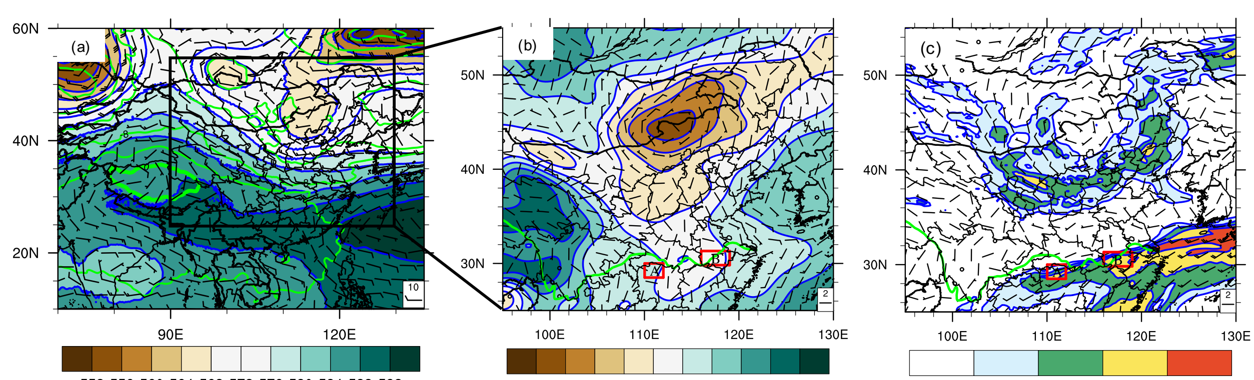

Figure 2. Horizontal distribution of (a) synoptic characteristics at 500 hPa (unit: 10 m), (b) sea surface pressure (unit: hPa), and (c) wind field at 700 hPa (unit: $m \cdot s^{-1}$) basing on GDAS (Global Data Assimilation System) FNL (Final analysis) data, at 0000 UTC 28 June. The blue line with shaded colors in panel (a) represents geopotential height, and the green line represents temperature. The blue line with shaded colors represents sea surface pressure in panel (b) and that represents wind speed in panel (c). All vectors in those three panels represent wind. The green line in panel (b) and (c) indicates the path of the Yangtze River.

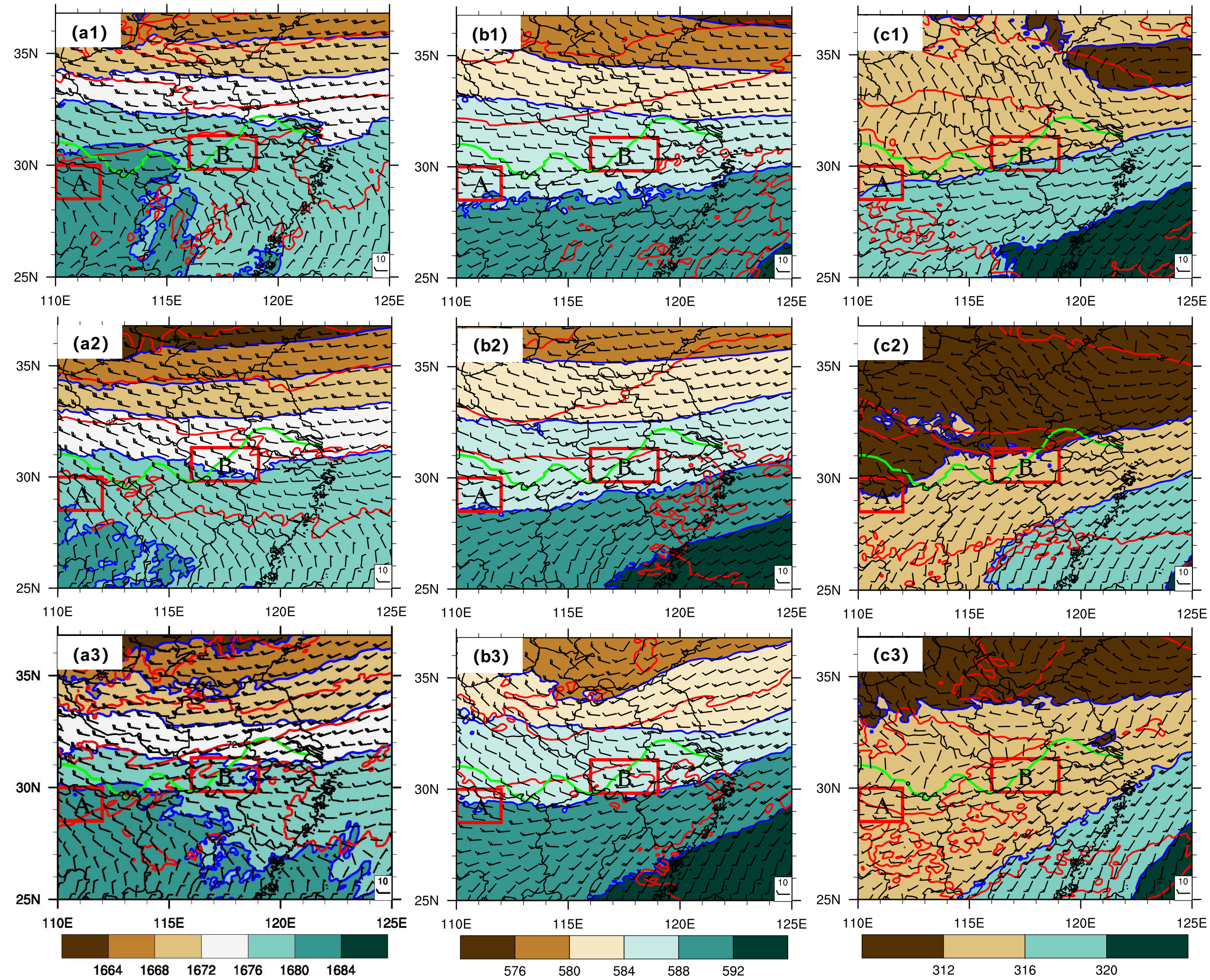

Figure 3. Horizontal distribution of simulated (a) geopotential height at 100 hPa (unit: 10 m), (b) geopotential height at 500 hPa (unit: 10 m), and (c) geopotential height at 700 hPa (unit: 10 m). Row 1 to 3 represent the geopotential height at 1200 UTC 27 June, 0000 UTC 28 June, and1200 UTC 28 June , respectively. The blue line with shaded colors in panel (a) and (b) represents geopotential height, and the red line represents temperature. All vectors in those three panels represent wind. The green line indicates the path of the Yangtze River.

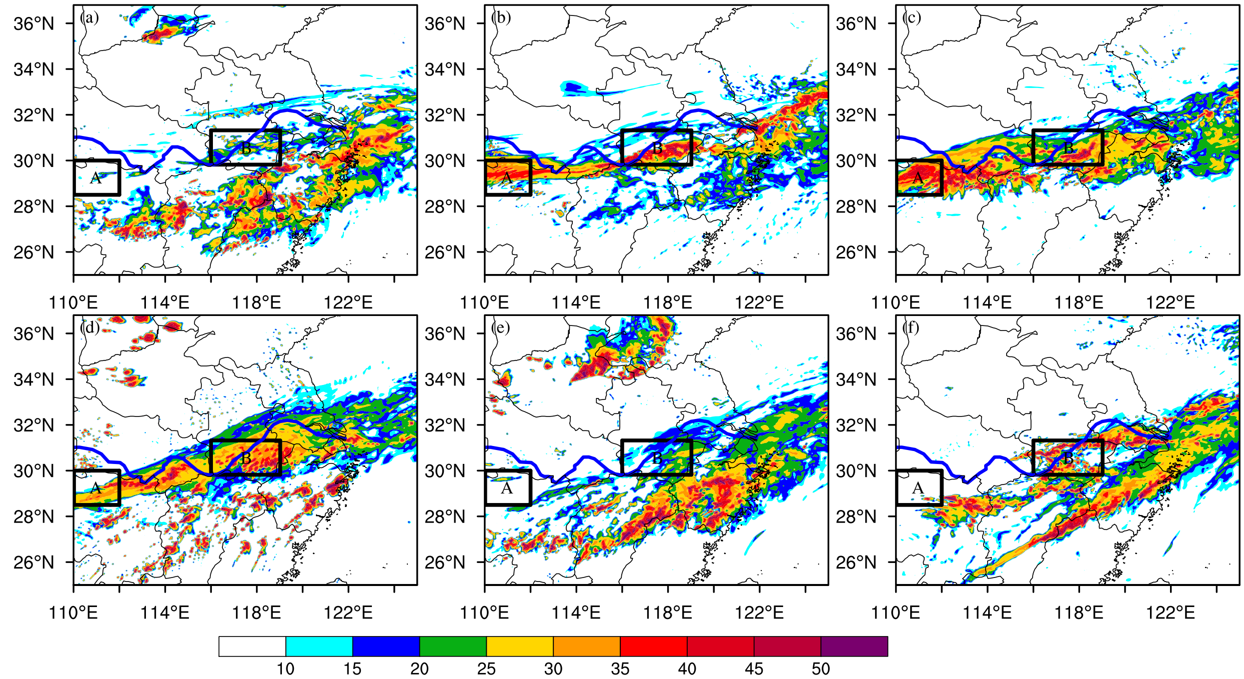

Figure 4. Horizontal distribution of maximum radar reflectivity (unit: dBZ) from 1200 UTC 27 June to 1800 UTC 28 June, with a 6 h interval. The blue line indicates the path of the Yangtze River.

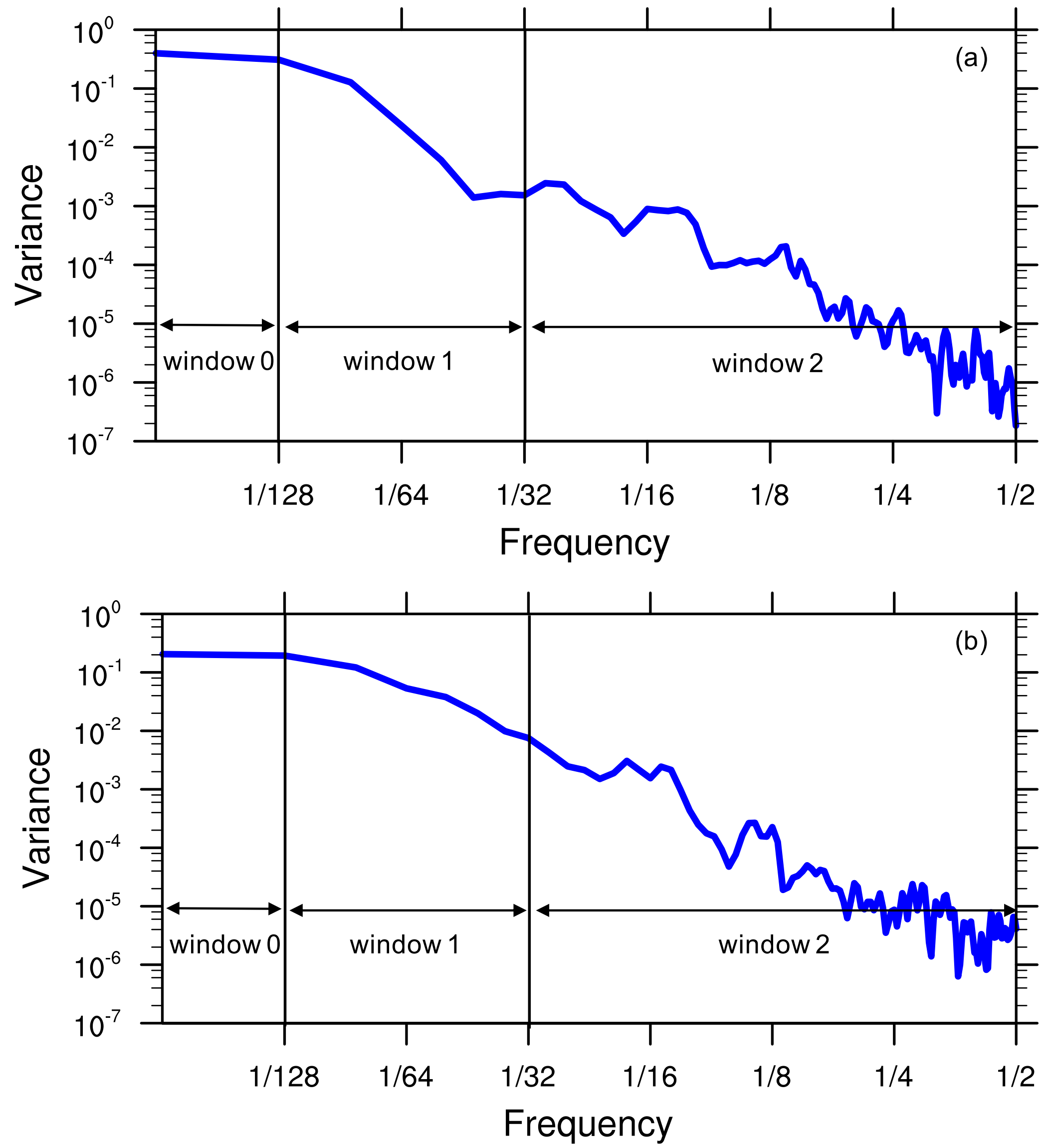

Figure 5. The spectrum of simulated vertical velocity at 700 hPa. Panel (a) and (b) represents domain A and B, respectively. X axis represents the Nyquist frequency.

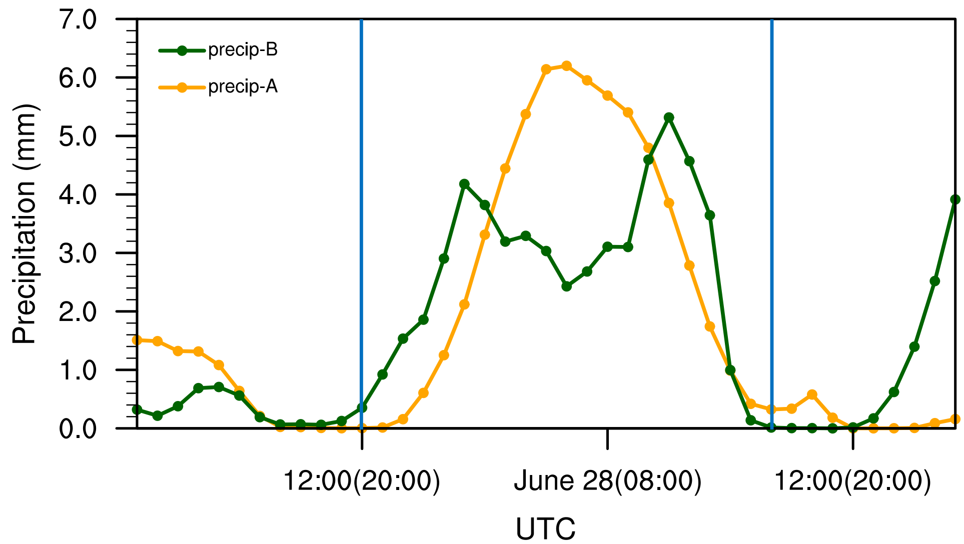

Figure 6. Variation of hourly precipitation in Domain A and Domain B (unit: mm). The blue line indicates the initial and terminal time of rainstorm period discussed in the study. Local time is marked within the parentheses in X axis.

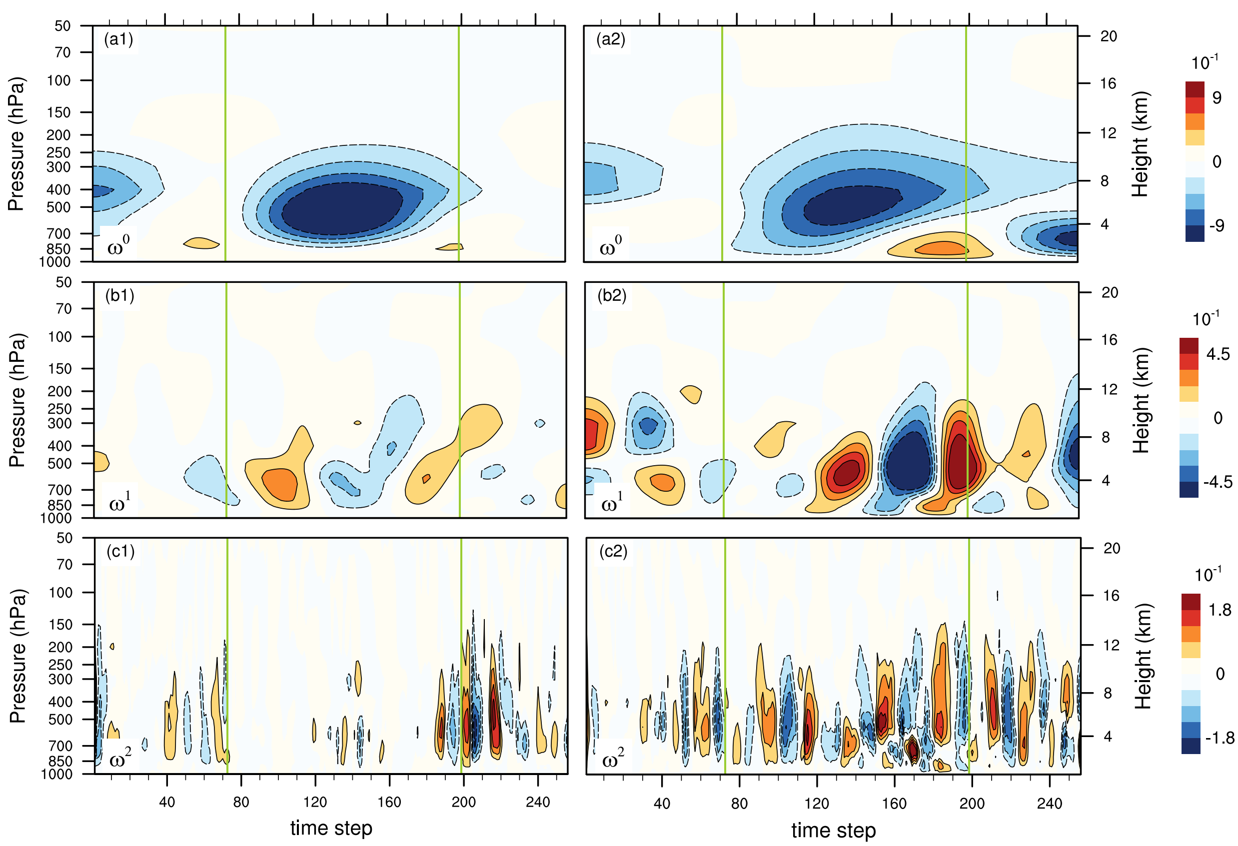

Figure 7. The pressure-time diagram of vertical velocity at pressure coordinate (unit: $\mathrm{Pa} \cdot \mathrm{s}^{-1}$) vs. time between different windows. The x axis consists of 256 time steps between 0000 UTC 27 June to 1830 UTC 28 June in a 10 min interval. The green line indicates the initial and terminal time of rainstorm. The left column is for Domain A and the right is for Domain B. Row 1 to 3 denotes vertical velocity of background flow window, mesoscale window, and rainstorm window, respectively.

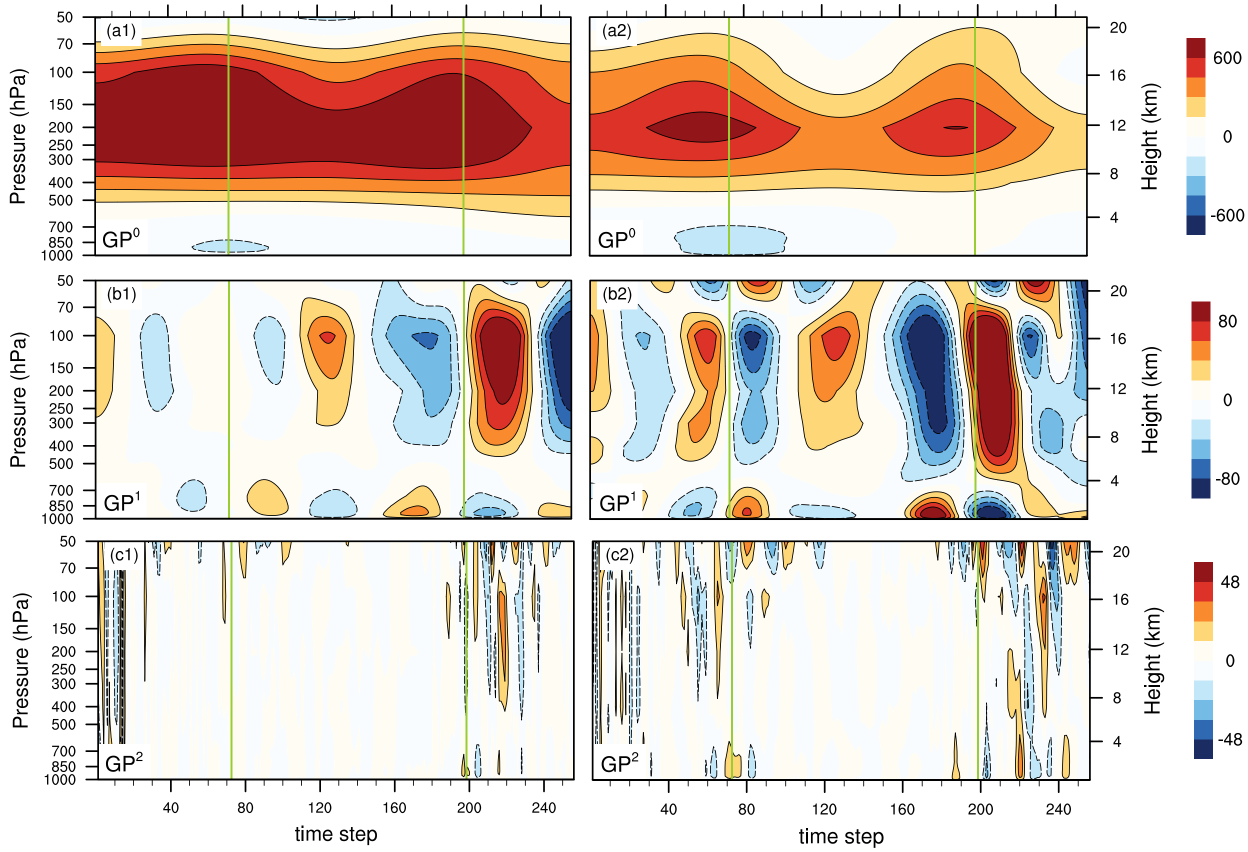

Figure 8. Same as Figure 6, except for geopotential (unit: $\mathrm{J \cdot kg^{-1}}$).

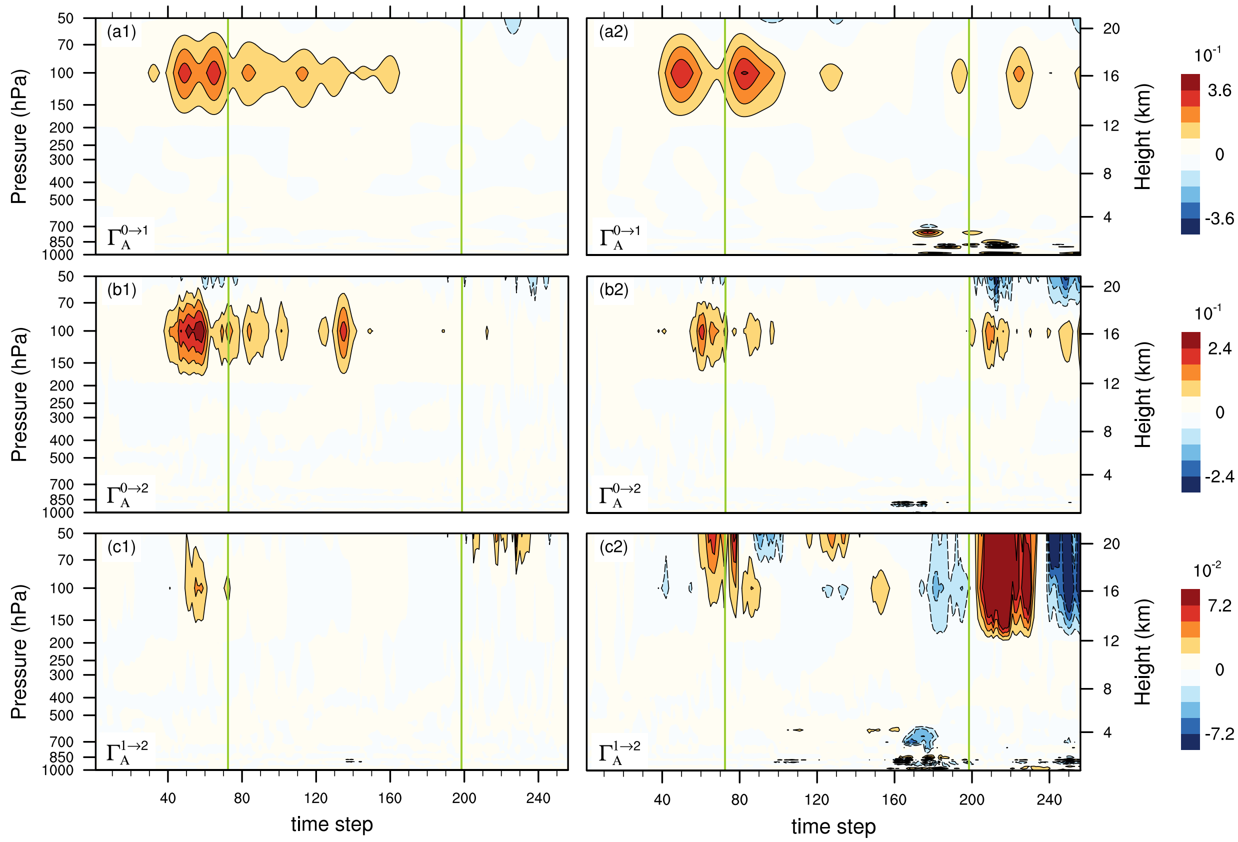

Figure 9. The pressure-time diagram of baroclinic canonical transfer Γ_A (unit: $m^2 \cdot s^{-3}$) vs. time. The x axis consists of 256 time steps between 0000 UTC 27 June to 1830 UTC 28 June in a 10 min interval. The green line indicates the initial and terminal time of rainstorm. The left column is for Domain A and the right is for Domain B. Row 1 to 3 denotes baroclinic canonical transfer between different scale windows. The superscript of Γ_A indicates the direction of baroclinic canonical transfer (e.g., $\Gamma_A^{0\to1}$ is from window 0 to window 1).

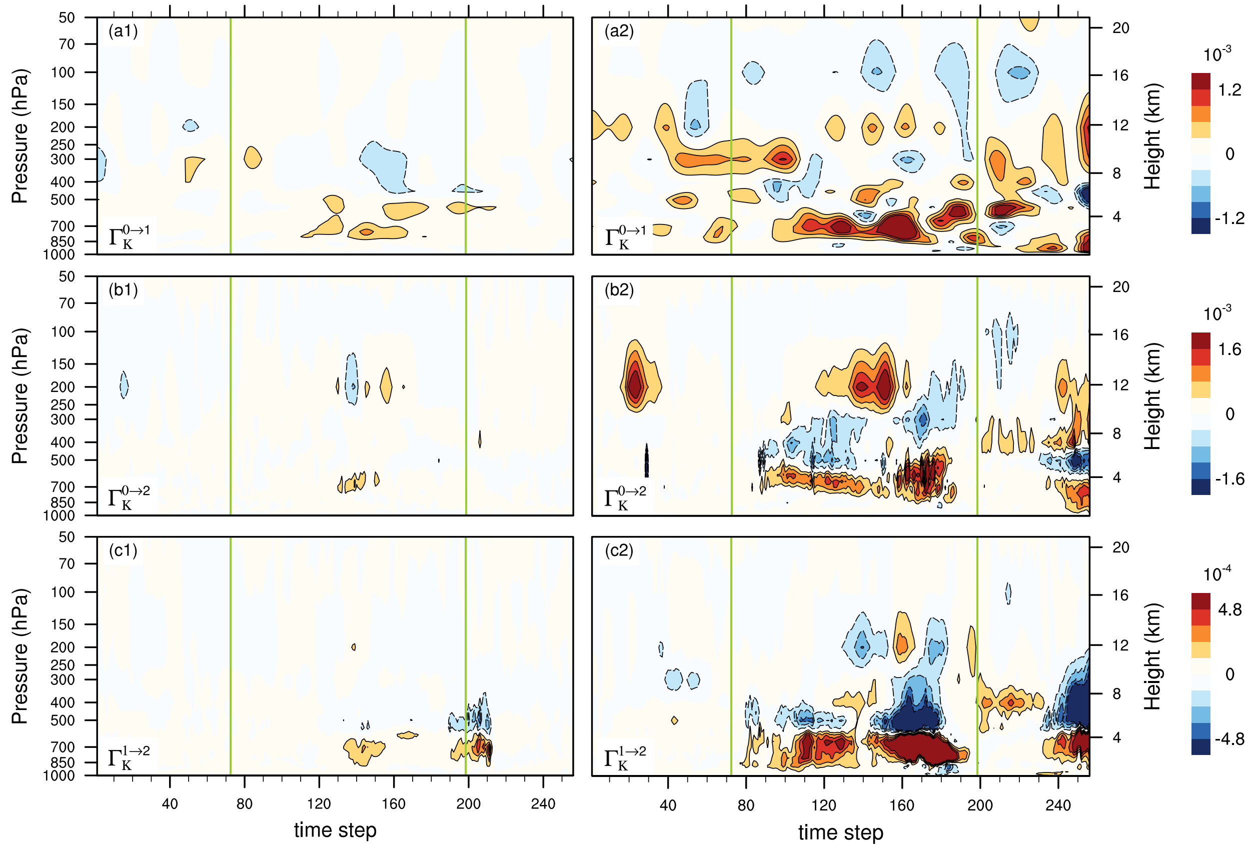

Figure 10. Same as Figure 9, except for the barotropic canonical transfers (unit: $m^2 \cdot s^{-3}$). The superscript of Γ_K indicates the direction of barotropic canonical transfer (e.g., $\Gamma_K^{0\to1}$ is from window 0 to window 1).

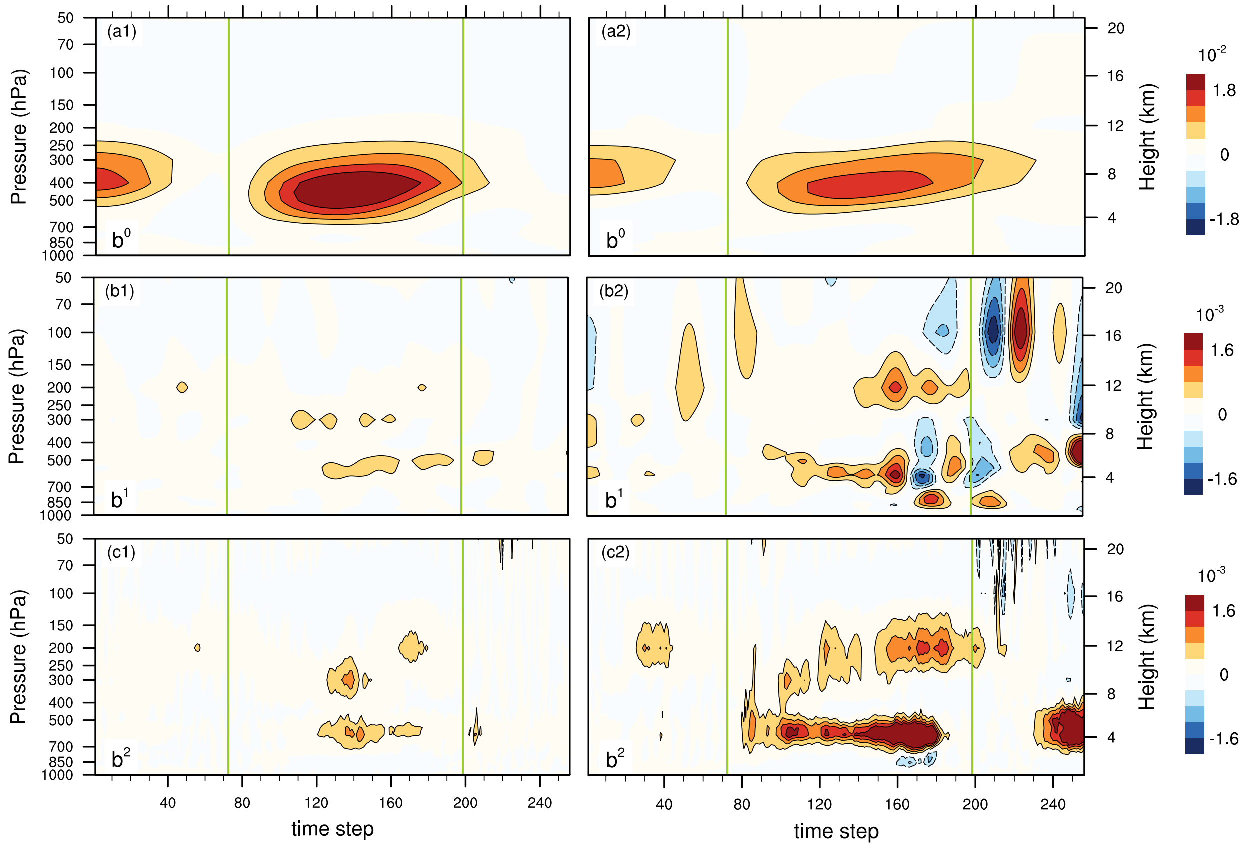

Figure 11. Same as Figure 9, except for buoyancy conversion rate.

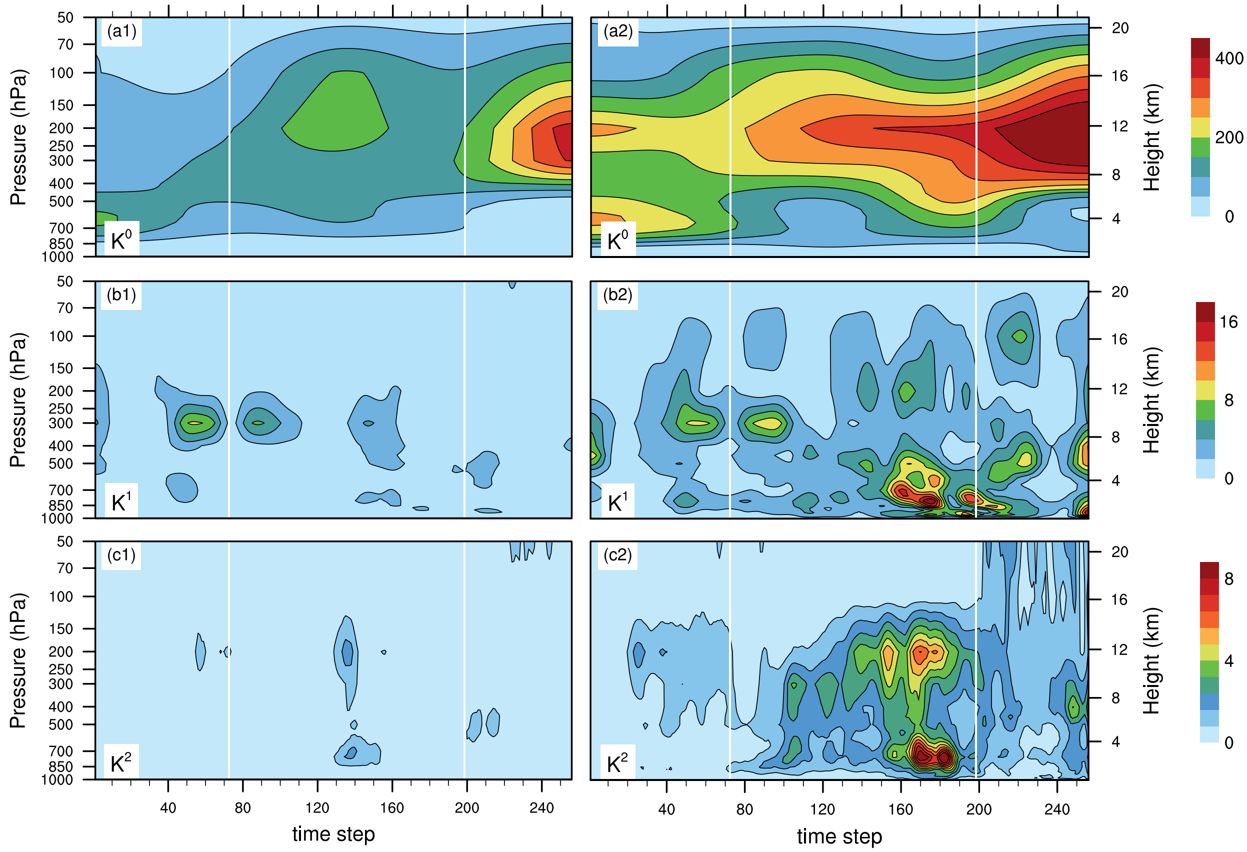

Figure 12. Same as Figure 12, except for kinetic energy (unit: $m^2 \cdot s^{-2}$). The white line indicates the initial and terminal time of rainstorm.

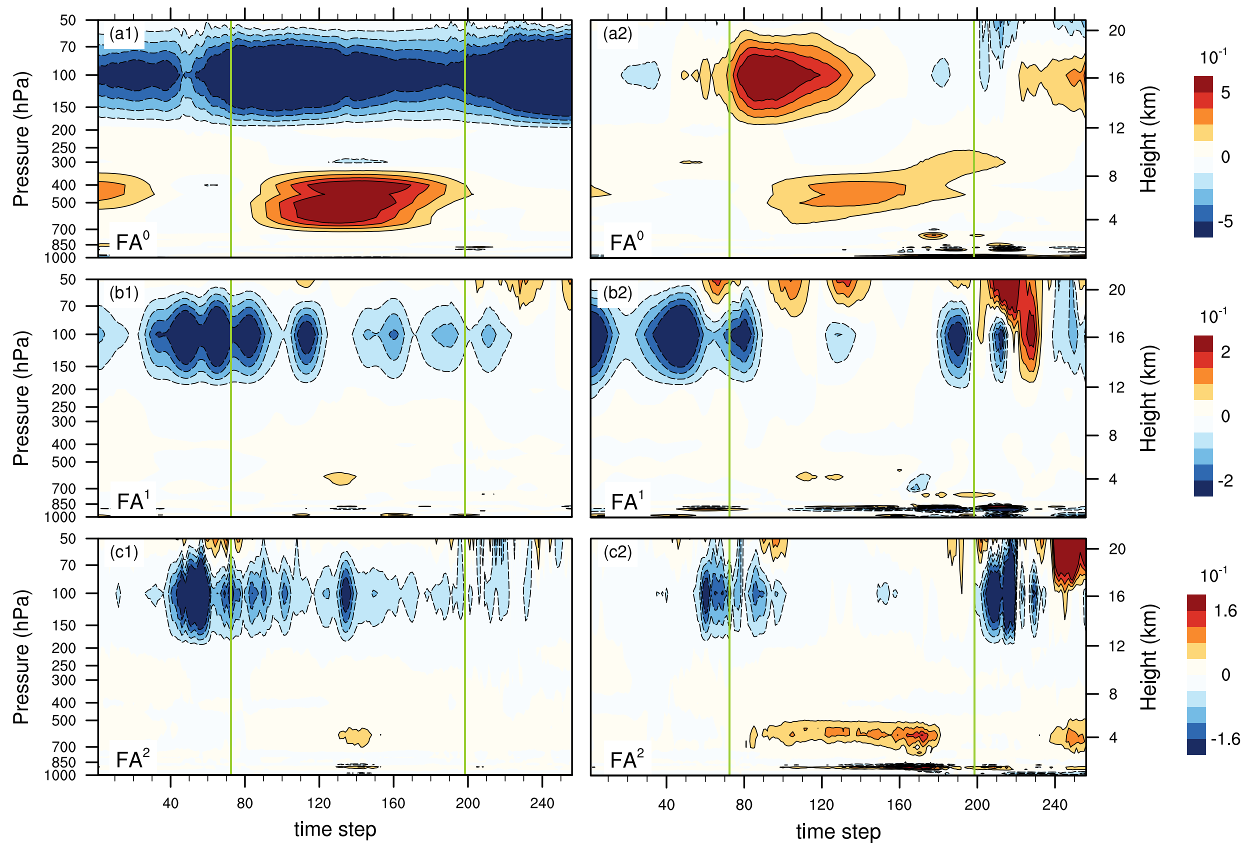

Figure 13. Same as Figure 12, except for F_A^{ϖ} (unit: $\mathrm{m}^2 \cdot \mathrm{s}^{-3}$).

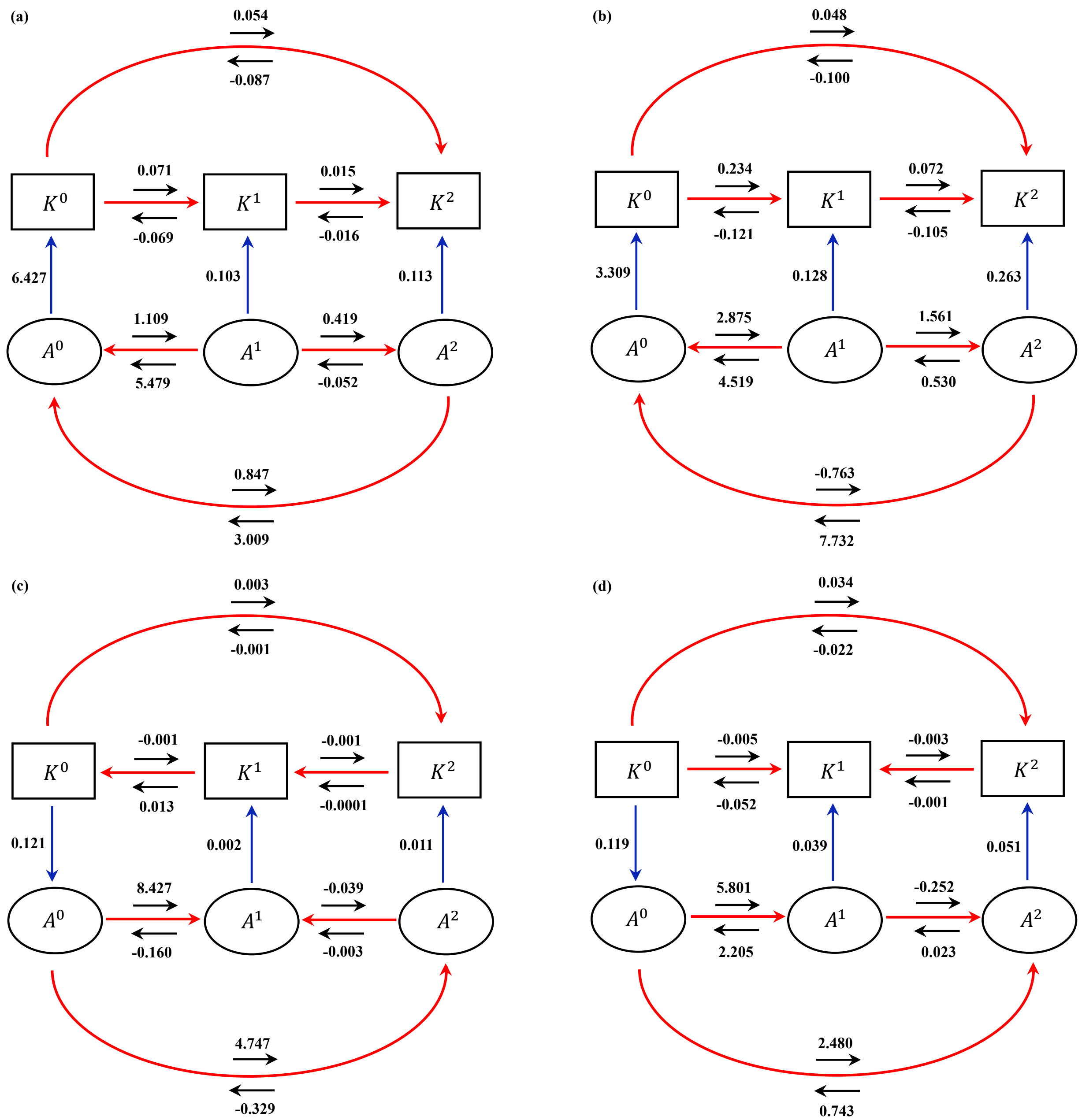

Figure 14. Lorenz energy circulation chart (unit: $10^2 \cdot \mathrm{W} \cdot \mathrm{m}^{-1} \cdot \mathrm{s}^{-2}$). (a) and (b) are respectively for Domain A and Domain B below 300 hPa. (c) and (d) are respectively for Domain A and Domain B above 300 hPa. K represents KE and A represents APE, with the superscript indicating different scale window. The red arrow represents the flow direction of baroclinic and barotropic canonical transfer. The blue arrow represents the buoyancy conversion direction within each scale window.

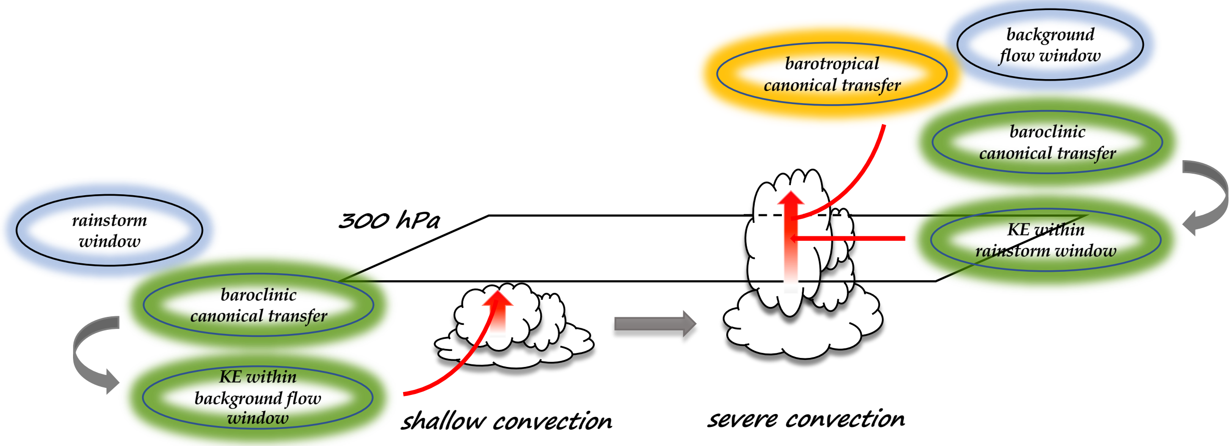

Figure 15. A conceptual model for kinetic energy source associated with a Meiyu-Baiu rainstorm.

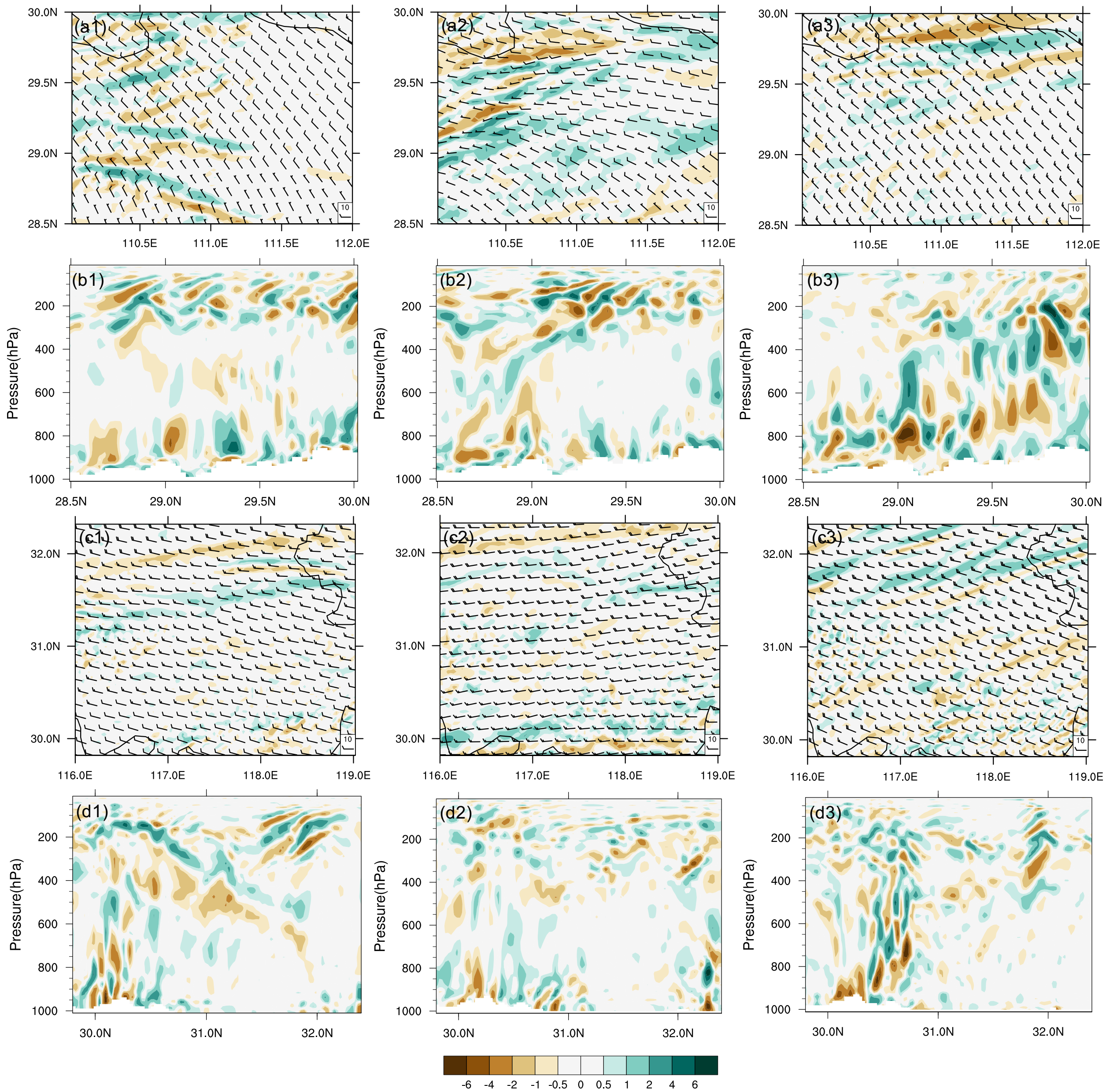

Figure 16. Horizontal and vertical distribution of divergence (unit: 10-5 s^{-1}) in domain A (Row 1 to 2) and domain B (Row 3 to 4). Column 1 to 3 are the divergence distribution at t=36, t=60, t=120 (referring to the X axis in Figure 6). Panel (a1) to (a3) are the horizontal distribution of divergence at 100 hPa in domain A. Panel (b1) to (b3) are the cross section of divergence along 110.5° E. Panel (c1) to (c3) are the horizontal distribution of divergence at 100 hPa in domain B. Panel (d1) to (d3) are the cross section of divergence along 118.5° E.

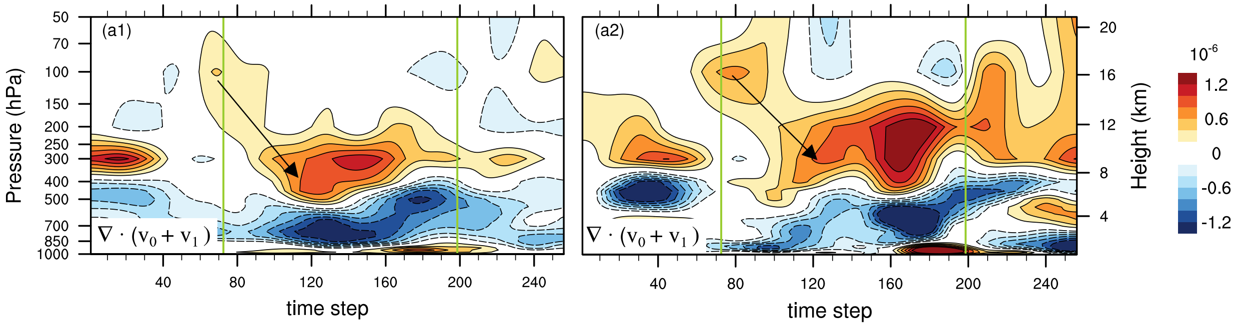

Figure 17. The pressure-time diagram of wind divergence (sum of background flow window and mesoscale window, unit: s^{-1}). The x axis consists of 256 time steps between 0000 UTC 27 June to 1830 UTC 28 June in a 10 min interval. The green line indicates the initial and terminal time of rainstorm. (a1) is for Domain A and (a2) is for Domain B.